

20 Abstract

21 Aerosol hygroscopicity plays a vital role in aerosol radiative forcing. One key parameter
22 describing hygroscopicity is the scattering enhancement factor, $f(\text{RH})$, defined as the ratio of
23 the scattering coefficient at humidified relative humidity (RH) to its dry value. Here, we utilize
24 the $f(80\%)$ from ORACLES 2016 and 2018 airborne measurements to investigate the
25 hygroscopicity of aerosols, its vertical distribution, its relationship with chemical composition,
26 and its sensitivity to organic aerosol (OA) hygroscopicity over the South-East Atlantic (SEA)
27 Ocean during the biomass burning (BB) season.

28 We found that aerosol hygroscopicity remains steady above 2 km, with a mean $f(80\%)$ of
29 1.40 ± 0.17 . Below 2 km, aerosol hygroscopicity increases with decreasing altitude, with a mean
30 $f(80\%)$ of 1.51 ± 0.22 , consistent with higher values of BB aerosol hygroscopicity found in the
31 literature. The hygroscopicity parameter of OA (κ_{OA}) is retrieved from the Mie model with a
32 mean value of 0.11 ± 0.08 , which is in the middle to upper range compared to literature. Higher
33 OA hygroscopicity is related to aerosols that are more aged, oxidized, and present at lower
34 altitudes. The enhanced BBA hygroscopicity at lower altitudes is mainly due to a lower OA
35 fraction, increased sulphate fraction, and greater κ_{OA} at lower altitudes.

36 We propose a parameterization that quantifies $f(\text{RH})$ with chemical composition and κ_{OA} based
37 on Mie simulation of internally mixed OA-(NH₄)₂SO₄-BC mixture. The good agreement
38 between the predictions and the ORACLES measurements implies that the aerosols in the SEA
39 during the BB season can be largely represented by the OA-(NH₄)₂SO₄-BC internal mixture
40 with respect to the $f(\text{RH})$ prediction. The sensitivity of $f(\text{RH})$ to κ_{OA} indicates that applying a
41 constant κ_{OA} is only suitable when the OA fraction is low and κ_{OA} shows limited variation.
42 However, in situations deviating these two criteria, κ_{OA} can notably impact scattering

43 coefficients and aerosol radiative effect; therefore, accounting for κ_{OA} variability is
44 recommended.

45 **Keywords:** hygroscopicity, biomass burning aerosol, chemical composition, κ_{OA} , Atlantic,
46 airborne measurements, parameterization

47

48 **1 Introduction**

49 Aerosol hygroscopicity is an important physicochemical property of atmospheric
50 aerosols, representing the extent to which particles take up water when exposed to a certain
51 relative humidity (RH) (Covert et al., 1972). Key parameters describing aerosol hygroscopicity
52 include the scattering enhancement factor, $f(\text{RH})$, which represents the enhancement of the
53 aerosol light-scattering coefficient as a function of RH (Carrico et al., 2003), and κ , the
54 hygroscopicity parameter, whose value is defined by its effect on the water activity of the
55 solution (Petters and Kreidenweis, 2007). Water uptake will increase the size and the mass of
56 hygroscopic aerosols, alter their refractive index, enhance the scattering ability, and ultimately
57 influence the single scattering albedo and aerosol radiative forcing (Cotterell et al., 2017; Titos
58 et al., 2021; Zieger et al., 2013). Furthermore, hygroscopicity affects aerosols' ability to act as
59 CCN (cloud condensation nuclei) and ice nuclei, and further influences cloud properties and
60 precipitation (Cai et al., 2021; Che et al., 2017; Ervens et al., 2007). Climate model results
61 show that even a modest change in κ_{OA} (κ of organic aerosols) can lead to significant changes
62 in CCN, droplet number concentration, and aerosol radiative effects (Liu and Wang, 2010;
63 Rastak et al., 2017). The treatment of aerosol hygroscopicity is one of the key factors
64 contributing to discrepancies between model simulations and observations and among model
65 estimates (Burgos et al., 2020; Haywood et al., 2008; Reddington et al., 2019).

66 Africa emits $\sim 1/3$ of the Earth's annual BB emissions (van der Werf et al., 2010), and
67 its burned areas are increasing every year (Andela et al., 2017). Each Austral spring (July to
68 October), the BB aerosols (BBA) from African fires are transported westward through the free
69 troposphere (FT) over the persistent stratocumulus cloud deck in the South-East Atlantic
70 (SEA), and eventually subside into the marine boundary layer (MBL) (Redemann et al., 2021).
71 BBA undergo atmospheric processing during transport, altering their chemical composition,
72 oxidation extent, particle polarity, molecular weight, volatility, and solubility (Rastak et al.,

73 2017), making the hygroscopicity highly variable. Laboratory studies show that minutes-old
74 BBA are more hygroscopic than hour-old BBA (Day et al., 2006), while the hygroscopicity of
75 BBA transported for more than several days in the SEA region remains an area of investigation.
76 Furthermore, these BBA mix with pristine aerosols and are subject to marine influences from
77 the SEA, resulting in a distinct vertical variation of aerosol hygroscopicity.

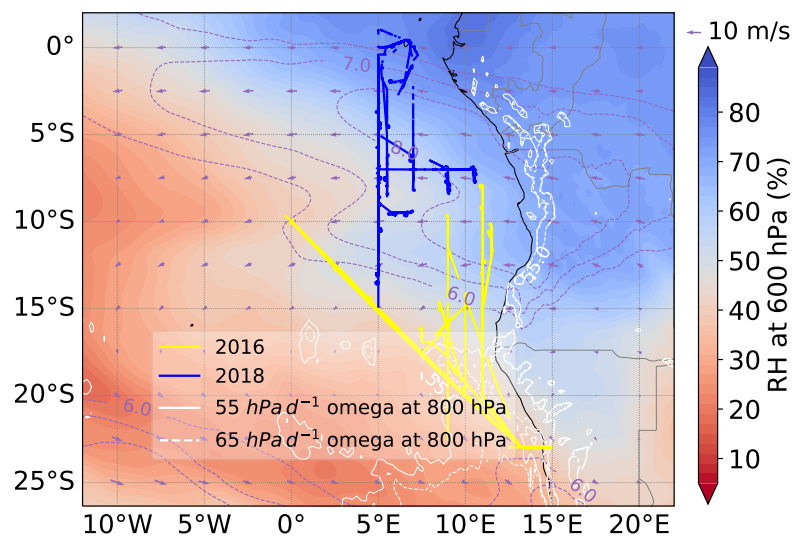
78 The hygroscopicity of organic aerosol (OA), the dominant component of aerosols in
79 most cases, is poorly characterized due to its chemical complexity (Kuang et al., 2020; Mei et
80 al., 2013). Values of κ_{OA} can range from 0 for hydrophobic freshly emitted organics to
81 approaching 1.0 for very hygroscopic amino acids (Kuang et al., 2020; Petters et al., 2009;
82 Zhang et al., 2007). BBOA are usually regarded as hydrophobic, while the mass fraction of
83 aged BBOA show a positive correlation with κ_{OA} (Cerully et al., 2015; Kuang et al., 2021).
84 Several studies have found a linear correlation between OA hygroscopicity and its oxidation
85 level, commonly characterized by the oxygen-to-carbon (O/C) ratio or the fraction of total
86 organic mass spectral signal at m/z 44 (f_{44}) (Lambe et al., 2011; Mei et al., 2013). However,
87 this linear relationship is not always established, especially for secondary OA with a lower O/C
88 ratio under sub-saturated conditions, for which solubility may play a more important role. In
89 addition, studies show molecular weight, surface tension, and liquid-liquid phase separation
90 are also related to the water affinity of OA (Liu et al., 2018; Rastak et al., 2017; Wang et al.,
91 2019), all contributing to the complexity of OA hygroscopicity.

92 The ORACLES (ObseRvations of Aerosols above CLouds and their intEractionS)
93 campaign (Redemann et al., 2021) provides a comprehensive observation of aerosols above the
94 SEA Ocean with 4-12 days of transport from Africa fires, making it a valuable opportunity to
95 investigate the hygroscopicity of aged BBA and their OA. In this paper, we first characterize
96 the aerosol hygroscopicity and its vertical distribution over the SEA during the BB season, then
97 propose a parameterization relating aerosol hygroscopicity with chemical composition and κ_{OA} ,

98 and finally evaluate the sensitivity of aerosol hygroscopicity to k_{OA} . Results are expected to
99 provide a reference to the treatment of aerosol hygroscopicity in climate models and satellite
100 retrievals, and to contribute to aerosol-cloud-interactions and radiative assessments in this
101 climatically important SEA region.

102 2 Methods

103 2.1 Aircraft Instrumentation and Data Analysis



104

105 Figure 1. Flight tracks in 2016 and 2018 ORACLES campaigns. Map of October mean of
106 ERA5 600 hPa RH overlaid by the 600 hPa zonal wind (purple contours; 6, 7, and 8 m s⁻¹),
107 600 hPa horizontal wind vector (purple arrows; m s⁻¹), and ORACLES flight tracks in 2016
108 (yellow) and 2018 (blue), respectively. White contours are the 2016 September mean vertical
109 velocity, omega, at 800 hPa. Solid and dashed lines represent the subsidence of 55 and 65
110 hectopascals per day (hPa d⁻¹).

111 We analyzed airborne, in situ data measured over the SEA region from the ORACLES
112 campaign performed in September 2016 and October 2018 (Redemann et al., 2021). The flight
113 tracks are shown in Fig. 1. All instruments were deployed on the NASA P-3 aircraft. Aerosol
114 particles were introduced into the P-3 via the solid diffuser inlet. The inlet was operated

115 isokinetically by matching the flow rate to the external air flow velocity to within 5% (Dobracki
116 et al., 2023). This inlet was designed to effectively transfer particles up to 4.0 μm dry diameter
117 (McNaughton et al., 2007). The inner pipework was designed for minimal transport losses for
118 particles up to 4.0 μm using an online particle loss calculator (Aerosol Calculator,
119 https://tsi.com/getmedia/540a30fa-8444-49f6-814f-891495c70aa1/Aerocalc2001_1). Two
120 Radiance Research M903 integrating nephelometers (Neph) were operating in parallel, one
121 (referred to as the ‘reference Neph’) under relatively dry conditions and the other (known as
122 the ‘humidified Neph’) maintained at $\sim 80\%$ RH. Particles entering the reference Neph were
123 heated to the aircraft cabin temperature, significantly reducing their RHs in the Neph and
124 resulting in most particles having an RH below 35%. The humidified Neph was situated
125 downstream of a humidifier, which maintained the RH at the inlet of the Neph at $\sim 80\%$ within
126 a few percent, as detailed in Howell et al. (2006). The RH probes in M903 were corrected based
127 on lab calibrations and the RH errors are roughly 3%. The temperature errors are about 0.5°C .
128 Measurements were reported at 1 Hz. For the calculation of $f(\text{RH})$, data with a reference Neph
129 RH greater than 35% or a humidified Neph RH smaller than 76% were excluded. The
130 distribution of the RHs of both the reference and humidified Neph used in this study are shown
131 in Fig. S3 in the supplementary material. Calibrations were performed in the field with
132 refrigerant R-134A (1,1,1,2-tetrafluoroethane). Truncation correction was performed for both
133 Neph according to Anderson and Ogren (1998). All scattering coefficients and scattering
134 enhancement factors are reported at 540 nm wavelength.

135 The non-refractory submicron aerosol composition was provided by a High-Resolution
136 Time-of-Flight Aerosol Mass Spectrometer (HR-ToF-AMS, Aerodyne Research Inc.)
137 (Dobracki et al., 2023). The fragment analysis provided f_{44} and f_{60} , representing the fractions
138 of the OA mass spectrum signals at $m/z=44$ (mainly CO_2^+) and $m/z=60$ (mainly $\text{C}_2\text{H}_4\text{O}_2^+$),
139 respectively, in the total OA mass. The mass concentration of refractory BC was provided by

140 a single particle soot photometer (SP2, Droplet Measurement Technology, Sedlacek et al.,
141 2022).

142 The dry particle number size distribution (PNSD) of PM₁ was provided by an ultra-
143 high-sensitivity aerosol spectrometer (UHSAS, Droplet Measurement Technology). The
144 UHSAS was calibrated with polystyrene latex (PSL) spheres, whose real refractive index n is
145 1.572 at the UHSAS laser wavelength (Howell et al., 2021). The UHSAS undersized particles
146 in BB plumes; the undersized data were corrected according to Howell et al. (2021). The PNSD
147 of super-micron particles was measured by an aerodynamic particle sizer (APS). The
148 aerodynamic diameter of APS was converted to the volume equivalent diameter according to
149 DeCarlo et al. (2004). Particles were assumed to be spherical (shape factor = 1) with a density
150 of 1.5 g cm⁻³. However, since the super-micron particles made a minimal contribution to the
151 total scattering coefficient, we have neglected the super-micron particles, and only UHSAS
152 measurements are used in this study. The minor contribution of super-micron particles to the
153 total scattering coefficients is described and illustrated in Section S1 and Fig. S1 in the
154 supplement. The aerosol/plume age was modelled with a two-week forecast using the Weather
155 Research and Aerosol Aware Microphysics (WRF-AAM) model (Thompson and Eidhammer,
156 2014). Carbon monoxide was tagged as tracer at the fire source, identified by a burned area
157 product from the moderate resolution imaging spectrometer with a 500 m spatial resolution.

158 All measurements were averaged to 15 s and adjusted to STP conditions at 273.15 K
159 and 1013 hPa. Data with scattering coefficient < 10 Mm⁻¹ are not included. The final
160 measurements used in this study have an average RH of 79±0.5 % for the humidified Neph and
161 RH<30 % for the reference Neph. To ensure the influence of BB emissions, only data with
162 $f_{60}>0.003$ are considered (Cubison et al., 2011). This study analyzes measurements from 21
163 flights, totaling approximately 134 flight hours after applying the abovementioned constraints.

164 2.2 Calculation of $f(\text{RH})$ and γ parameterization

165 The aerosol scattering enhancement factor, $f(\text{RH})$, is calculated as:

$$f(\text{RH}) = \frac{\sigma_{\text{sp}}(\text{RH})}{\sigma_{\text{sp}}(\text{RH}_{\text{ref}})} \quad (1)$$

166 where $\sigma_{\text{sp}}(\text{RH})$ and $\sigma_{\text{sp}}(\text{RH}_{\text{ref}})$ represent the scattering coefficients at humidified and reference
167 Neph RHs, respectively. Note the $f(\text{RH})$ only include those with reference Neph RHs equal to
168 or smaller than 35 % to facilitate comparison with previous studies. For simplicity, we denote
169 the $f(\text{RH})$ at the RH of humidified Neph as $f(80\%)$, despite the small variation of the RH in
170 humidified Neph. The $f(\text{RH})$ is usually fitted to a γ parameterization to apply to a more
171 extensive RH range (Sheridan et al., 2002; Titos et al., 2016):

$$f(\text{RH}) = \left(\frac{1 - \text{RH}/100}{1 - \text{RH}_{\text{ref}}/100} \right)^{-\gamma} \quad (2)$$

172 In our case, the γ was calculated with the RH and RH_{ref} using Eq. 2 since the $f(\text{RH})$ was only
173 measured at a fixed RH.

174 2.3 Modeling of $f(\text{RH})$

175 The $f(\text{RH})$ can be modeled with the Mie theory (Mie, 1908). The Python package
176 PyMieScatt (Sumlin et al., 2018), an implementation of the Mie theory, was applied in this
177 study. Inputs of PyMieScatt include PNSD and complex refractive index. Dry particles beyond
178 PM_{10} (particulate matter with an aerodynamic diameter less than 1 μm) are not included in this
179 calculation, supported by their minor contribution to the total scattering, as discussed in Section
180 S1 of the supplement. A volume mixing rule was used to calculate the refractive index. The
181 volume of inorganic salts was converted from those of SO_4^{2-} , NO_3^- , and NH_4^+ from AMS
182 following a modified ion-pairing scheme (Gysel et al., 2007; Zhang et al., 2022). Good
183 agreement has been achieved for calculated and measured scattering coefficients under dry
184 conditions, which indicates good data quality and provides the basis for calculating $f(\text{RH})$ and
185 retrieving $\kappa_{f(\text{RH})}$. The comparison between calculated and measured scattering coefficients is
186 shown in Fig. S4 in the supplement. By combining Mie model with the κ -Köhler theory, we

187 can then calculate the scattering coefficients under humidified RH conditions. For more details
 188 of the calculation, refer to Zieger et al. (2013). Subsequently, $f(\text{RH})$ and γ can be obtained using
 189 Eq. 1 and 2. The theoretically calculated $f(\text{RH})$ in Sections 3.3.1 and 3.3.2 used an assumed
 190 PNSD and different chemical composition combinations. One assumed PNSD was used in
 191 these calculations due to its minor impact on $f(\text{RH})$, which has been discussed in detail in
 192 Section S2 in the supplement.

193 2.4 $\kappa_{f(\text{RH})}$ retrieval and κ_{OA} calculation

194 The aerosol hygroscopicity parameter κ can be retrieved from $f(\text{RH})$, usually denoted
 195 as $\kappa_{f(\text{RH})}$ (Chen et al., 2014). It can be regarded as the scattering coefficient weighted average κ
 196 (Kuang et al., 2021). Specifically, we iteratively adjust $\kappa_{f(\text{RH})}$ to minimize the difference
 197 between the calculated and measured $f(\text{RH})$. Detailed descriptions of the retrieval procedure of
 198 $\kappa_{f(\text{RH})}$ can be found in Chen et al. (2014).

199 According to Petters and Kreidenweis (Petters and Kreidenweis, 2007), the overall κ_{chem} ,
 200 which is defined as the κ for the whole aerosol population, can also be calculated from various
 201 chemical compositions following the ZSR (Zdanovskii-Stokes-Robinson) mixing rule. Kuang
 202 et al. (2020b) thoroughly outlined in Section 3.3 that the $\kappa_{f(\text{RH})}$ can accurately represent the κ_{chem}
 203 of PM_{10} . Therefore, the hygroscopicity parameter of OA, κ_{OA} , can be calculated as:

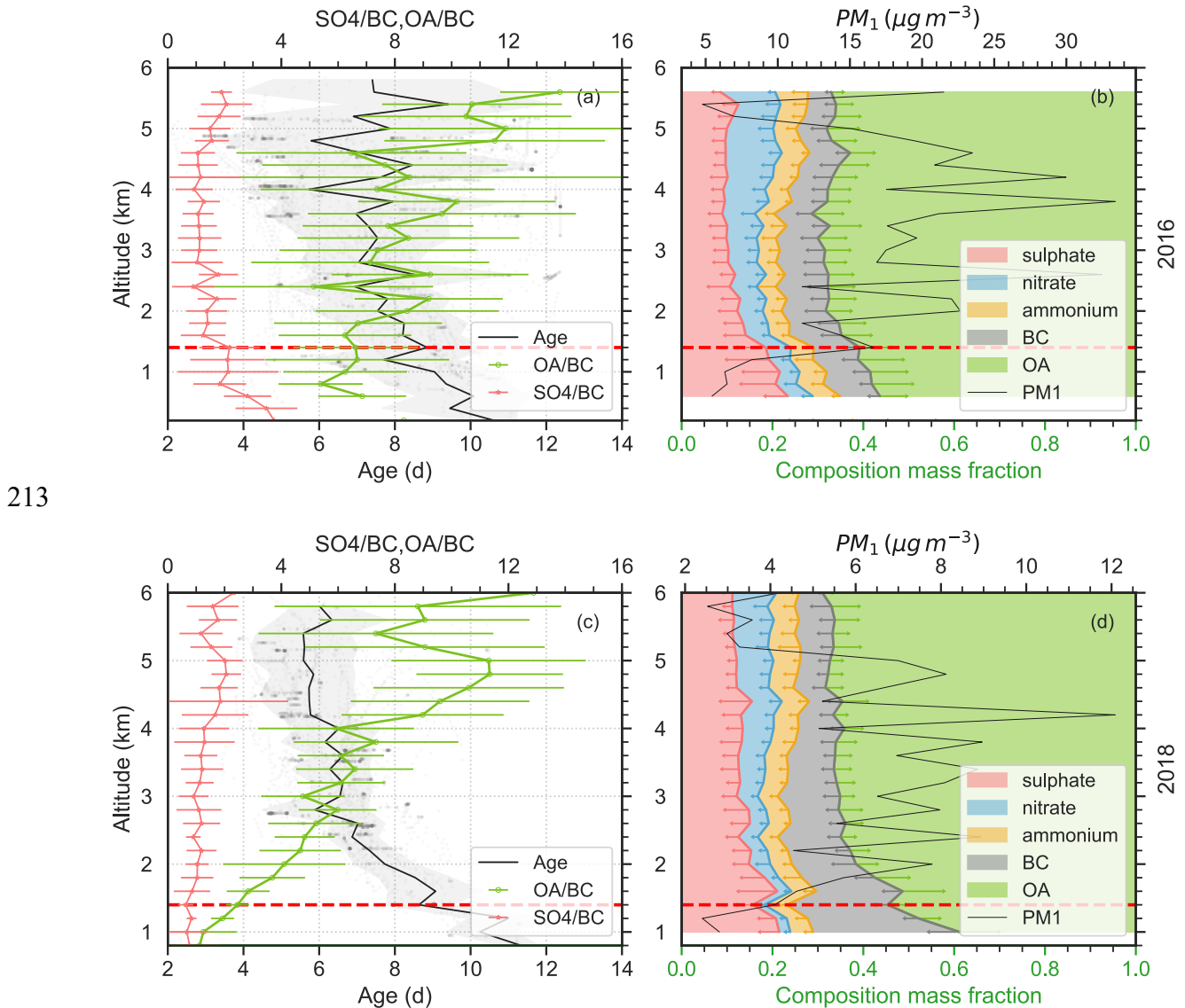
$$\kappa_{\text{OA}} = \frac{\kappa_{f(\text{RH})} - (\sum_{i=\text{inorg}} \kappa_i \varepsilon_i + \kappa_{\text{BC}} \varepsilon_{\text{BC}})}{\varepsilon_{\text{OA}}}, \quad (3)$$

204 where *inorg* represents inorganic salts, which were derived from the SO_4^{2-} , NO_3^- , and NH_4^+
 205 ions measured from AMS following a modified ion-pairing scheme (Gysel et al., 2007; Zhang
 206 et al., 2022). The subscript *i* denotes each individual inorganic salt. ε represents the volume
 207 fraction of each component, calculated as the ratio of the volume of each component to the
 208 volume of PM_{10} . The PM_{10} volume is computed as the sum of the volumes of inorganic salts,

209 OA, and BC. The hygroscopic parameter κ and density used in this study can be found in Table
 210 S1.

211 **3 Results and discussion**

212 **3.1 Overview of chemical compositions in 2016 and 2018 ORACLES**



214 Figure 2. The vertical distribution of plume age and chemical composition. (a, c) Variation of
 215 plume age (black), OA/BC, and SO4/BC with altitude in 2016 (upper) and 2018 (lower)
 216 ORACLES campaigns, respectively. Grey dots show the distribution of plume age with the
 217 altitude. (b, d) The average vertical distribution of the mass ratio of chemical compositions and
 218 the average mass concentration of PM₁ from AMS and SP2 in every 200 m in 2016 and 2018
 219

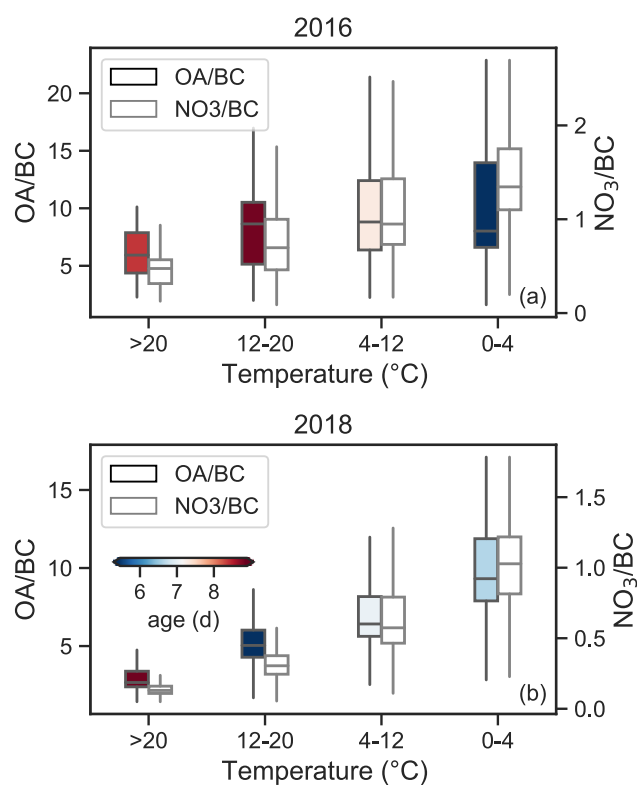
220 ORACLES campaigns, respectively. The lines are the mean value in every 200 m bin. Errorbars
221 and grey shading represent the standard deviation in every 200 m bin. The red dashed lines at
222 1400 m show the maximum height of the MBL during the study period.

223 Flights in 2016 ORACLES (Fig. 1, yellow lines) are in the region of 8-24° S and 0-15°
224 E, traversing both the southern African Easterly Jet (AEJ-S) region and the continent
225 anticyclone (Ryoo et al., 2021). As a result, aerosols around 3-4 km in 2016 ORACLES include
226 both less aged (<4 d) particles coming directly from the continent and highly aged (>10 d)
227 particles transported from the west/north, resulting in a larger variation of plume age in each
228 level as shown in Fig. 2a. At lower altitudes, aerosols are less aged than those in the 2018
229 campaign due to the subsidence (positive values of omega) near the Namibian coast (Fig. 1).
230 During the 2016 campaign, the cloud top is generally below 1.5 km. The 2018 ORACLES
231 flights, represented by blue lines in Fig. 1, are primarily situated within the 0-15° S and 5-10°
232 E coordinates. The cloud top in this region is a bit lower than in 2016 campaign, centering
233 around 1 km. This area generally coincides with the region influenced by the southern African
234 Easterly Jet (AEJ-S). BBA are lifted up to the free troposphere, transported westward by AEJ-
235 S and then subside into the marine boundary layer, rendering the distinct vertical age pattern
236 that increases with the decreasing altitude (Fig. 2c). Correspondingly, aerosols in the SEA
237 region during BB season exhibit distinct vertical distribution of chemical composition. From
238 Fig. 2b and 2d, the vertical profiles of chemical composition fractions are generally consistent
239 during 2016 and 2018 ORACLES campaigns. In this section, we focused on the variation of
240 OA and sulphate, two components that dominate aerosol hygroscopicity in the SEA.

241 OA constitutes the largest fraction of aerosol mass in ORACLES, approximately 60 %.
242 The OA mass fraction in both years shows little variation above 2 km; below this altitude, OA
243 mass fraction decreases with decreasing altitude, in contrast to the trend of the sulphate mass
244 fraction. The OA/BC ratio, representing the OA mass concentration normalised by that of BC

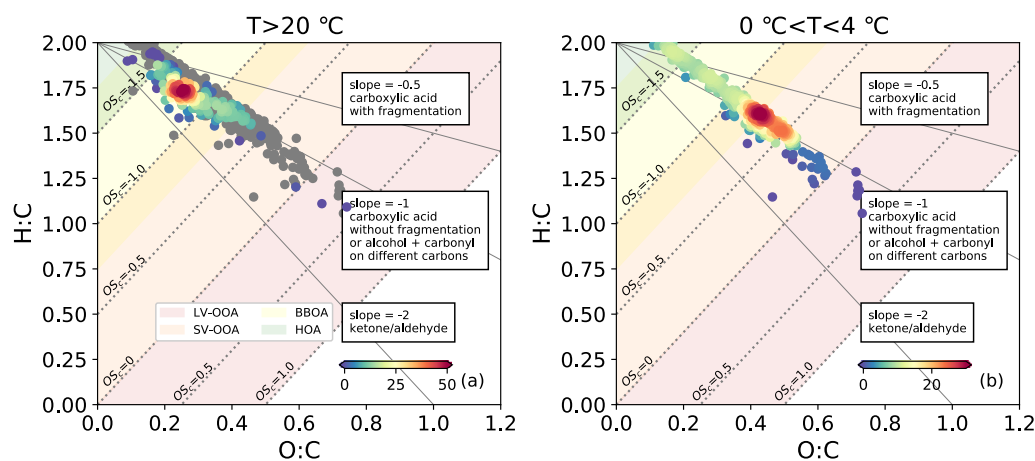
245 to remove the dilution effect during transport and an indication of OA processing, differs in
246 2016 and 2018. While 2018 data shows a clear decrease in OA/BC with decreasing altitude,
247 the decrease was less pronounced in 2016, showing considerable variation at identical altitudes.
248 In the meanwhile, the OA/BC shows a clear reverse trend with the plume age in 2018, this
249 inverse relationship is less obvious in 2016. Dobracki et al. (2022) used RH as an indicator to
250 investigate the importance of thermodynamic partitioning in OA/BC changes during the 2016
251 ORACLES campaign, concluding that it accounts for no more than 10 % of the changes. The
252 dominant factor is believed to be the oxidation of OA through fragmentation. A similar result
253 is found in this study using temperature as an indicator, as shown in Fig. 3a. Please note Fig. 3
254 only considers OA above 1.4 km and temperature > 0 °C to minimize the marine influence and
255 to exclude possible ice nucleation. The OA/BC ratio in the 2016 ORACLES campaign did not
256 show a clear decrease with increasing temperature, as NO_3/BC did, which is a result of
257 thermodynamic repartition to the gas phase. However, in the 2018 ORACLES campaign, we
258 did notice a significant decrease of OA/BC with increasing temperature (Fig. 3b). The OA/BC
259 decreased ~ 70 % from 9.7 ± 3.1 for temperature $0-4$ °C to 2.9 ± 0.9 for temperature > 20 °C, only
260 slightly lower than the decrease of NO_3/BC , ~ 85 %. Yet, we cannot simply attribute the OA/BC
261 changes to thermodynamic repartition while disregarding the effect of ageing or OA oxidation.
262 In 2018, temperature and plume age are closely correlated (Pearson correlation coefficient of
263 0.51), and the decrease in OA/BC is accompanied by ageing (Pearson correlation coefficient
264 of 0.57), as shown in Fig. 2a and b. We utilized the oxidation state to differentiate between the
265 effects of thermodynamic repartition and OA oxidation. Figure 4 shows the Van Krevelen
266 diagrams (H/C vs. O/C, Ng et al., 2011) for aerosols at temperatures > 20 °C and $0-4$ °C. The
267 estimated carbon oxidation state (OS_C), defined as $\text{OS}_\text{C} = 2\text{O}/\text{C} - \text{H}/\text{C}$, can also indicate different
268 OA volatility regimes, with OS_C of -2.0 – -1.5 for HOA (hydrocarbon-like OA), -1.75 – -0.75
269 for BBOA (biomass burning OA), -1.0 – 0.0 for SV-OOA (semi-volatile oxidized OA), and

270 0.0–1.0 for LV-OOA (low volatility oxidized OA) (Donahue et al., 2012; Kroll et al., 2011).
 271 If thermodynamic repartition plays a more crucial role, the OA remaining under higher
 272 temperature would be less volatile due to evaporation of more volatile OA. Notably, we found
 273 the opposite. From Fig. 4, aerosols at temperature > 20 °C (lower altitudes) are generally more
 274 volatile than those at temperature 0-4 °C (higher altitudes). This indicates that thermodynamic
 275 repartition is not a dominant factor in OA/BC changes, and that the OA oxidation through
 276 fragmentation is more important in OA/BC changes in 2018, consistent with the 2016
 277 campaign as well as results in Dobracki et al. (2022). This is also in line with the findings of
 278 Dang et al. (2022) which found less organics in aerosols collected on filters associated with
 279 more aged plumes and more rounded and viscous organics on filters sampled from less aged
 280 plumes. For OA below 1.4 km, aqueous phase reactions and cloud scavenging might also
 281 contribute to the loss of OA during the entrainment and within the MBL (Che et al., 2021; Wu
 282 et al., 2020).



283

284 Figure 3. OA/BC (black outline) and NO₃/BC (grey outline) mass ratios as a function of
 285 ambient temperature in 2016 (a) and 2018 (b) ORACLES campaign, for altitude > 1.4 km and
 286 temperature > 0 °C. The boxes represent the 10th percentile, 25th percentile, median, 75th
 287 percentile, and 90th percentile.



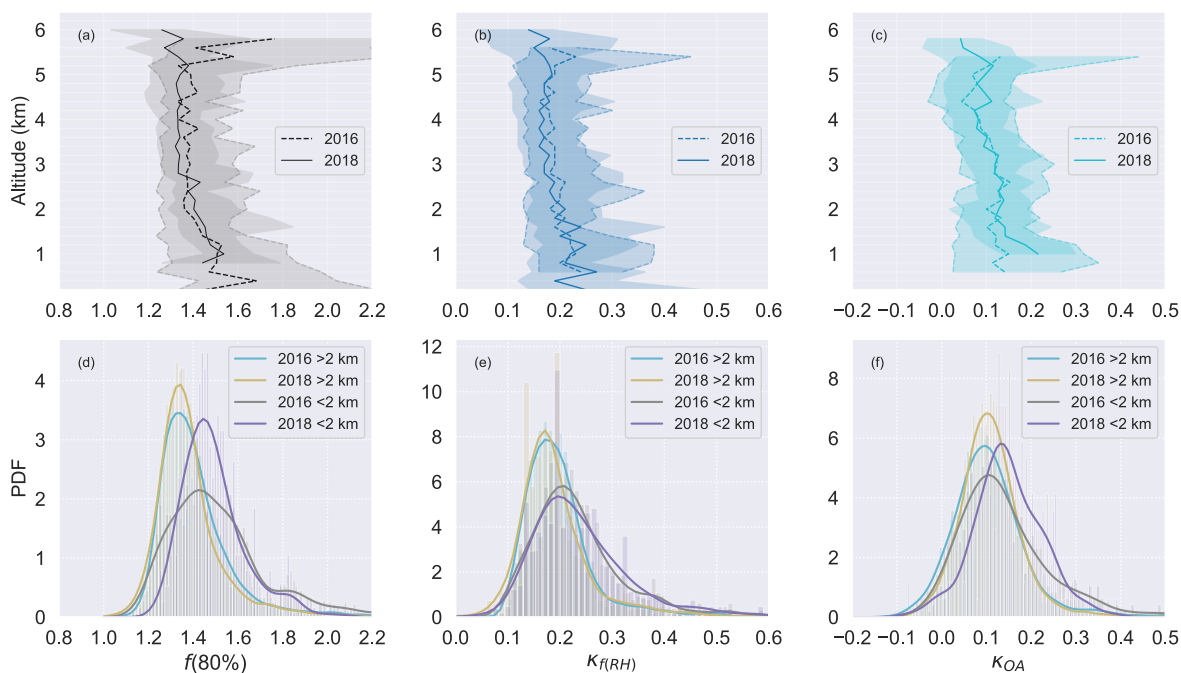
288
 289 Figure 4. Van Krevelen diagram (H/C vs. O/C) for aerosols with temperature higher than 20 °C
 290 (a) and with temperature lower than 4 °C (b). The color scale indicates the density of the data
 291 in each plot. The grey dots in (a) are the Van Krevelen diagram of aerosols with temperature
 292 lower than 4 °C, the same as (b).

293 The variation of sulphate mass fraction remains largely constant above 2 km, and below
 294 2 km, increases with decreasing altitudes. The higher sulphate fraction at lower altitudes is
 295 consistent with the observations from CLARIFY-2017 (CLOUD-Aerosol-Radiation Interaction
 296 and Forcing for Year 2017) campaign (Wu et al., 2020), which was conducted downwind of
 297 ORACLES in the SEA ocean. This higher sulphate fraction at lower altitudes results from the
 298 increase of SO₄/BC and decrease of OA/BC. SO₄/BC ratio generally remains constant above
 299 800 m in both years' campaign. However, for 2016 ORACLES campaign, where there are
 300 samples below 800 m, the ratio shows an increase with decreasing altitude. This increase could
 301 indicate a sulphate contribution from the ocean, either in the form of sea-salt sulphate or
 302 through the oxidation of dimethylsulfide (DMS) emitted by marine phytoplankton. The latter

303 can contribute to non-sea-salt sulphate by oxidizing to SO_2 and further to sulphate (Mayer et
 304 al., 2020; Alexander et al., 2005). Notably, part of the 2016 flight region, especially the SEA
 305 offshore of Namibia, is known as an upwelling region with high DMS emissions (Andreae et
 306 al., 1995). Klopper et al. (2020) have attributed 57 % of sulphate to sea salt and 43 % to non-
 307 sea-salt sulphate along the Namibian coast. These findings align with model simulations
 308 showing that DMS is the third largest CCN source in the SEA up to 2 km (Che et al., 2022b).

309 Furthermore, BC mass constitutes approximately 10 % of the PM_{10} mass fraction,
 310 indicating the large influence of BB in this region. The nitrate mass fraction increases with
 311 increasing altitude in all layers, which is consistent with the findings of CLARIFY, and can be
 312 explained by the shift of gas-particle partitioning of the $\text{HNO}_3\text{-NH}_3\text{-NH}_4\text{NO}_3$ system towards
 313 the aerosol phase at the lower temperatures found at higher altitudes (Wu et al., 2020). The
 314 mass fraction of ammonium stays stable with height, approximately 5 %. We neglected
 315 chloride in this study as it accounts for less than $1\pm 1\%$ mass fraction.

316 3.2 Aerosol hygroscopicity in SEA in 2016 and 2018 ORACLES



317

318 Figure 5. Vertical profiles and PDF of $f(80\%)$ (a, d), $\kappa_{f(RH)}$ (b, e), and κ_{OA} (c, f) for aerosols in
319 the 2016 (dotted line) and 2018 (solid line) ORACLES campaign. The lines in a, b, and c
320 represent the medians, and the shadings in a, b, and c represent the 10th and 90th percentiles.

321 In general, the aerosol hygroscopicity stays stable above 2 km in both years' campaigns;
322 while below 2 km, aerosols become more hygroscopic at lower altitudes (Fig. 5). The results
323 from the Levene's test for medians for $f(80\%)$, $\kappa_{f(RH)}$, and κ_{OA} indicate that $f(80\%)$, $\kappa_{f(RH)}$, and
324 κ_{OA} are statistically different above and below 2 km, with a confidence level of 95%. This is
325 consistent with the vertical variation of sulphate and OA mass fraction, i.e. more sulphate and
326 less OA at lower altitudes (Fig. S5). The probability density function (PDF) distributions of
327 $f(80\%)$ and $\kappa_{f(RH)}$ are similar in the 2016 and 2018 campaigns, with larger variations and higher
328 values of the aerosol hygroscopicity PDF under 2 km (Fig. 5d and 5e). For $f(80\%)$ below 2 km,
329 a primary mode with a value of around 1.45 is evident, but there is also a second mode with a
330 value of around 1.81 for aerosols in both years. While the second mode is subtle, it can be
331 identified in the PDF of $\kappa_{f(RH)}$ (Fig. 5e). This suggests the presence of highly hygroscopic
332 substances and could indicate marine influence, as most aerosols below 2 km are within the
333 MBL. For aerosols above 2 km, the mean and standard deviation of $f(80\%)$ and $\kappa_{f(RH)}$ are
334 1.40 ± 0.17 and 0.19 ± 0.07 , respectively (Fig. 5, Table 1, and Table S2). These values indicate
335 less hygroscopic particles (Liu et al., 2011) and are lower than those for marine aerosols (Zieger
336 et al., 2010; Carrico et al., 2003) but higher than those for dust and polluted dust particles
337 (Bukowiecki et al., 2016; Zhang et al., 2015a). They are comparable to smoke-dominated
338 aerosols, such as the smoke from savanna fires in Australia (Gras et al., 1999) and the BBA
339 from forest fires in the northeast US (Wang et al., 2007). These values are slightly higher than
340 the $f(80\%)$ in Brazil (SCAR-B) (Kotchenruther and Hobbs, 1998). The particles below 2 km
341 are more hygroscopic (Liu et al., 2011). The mean and standard deviation of $f(80\%)$ and $\kappa_{f(RH)}$
342 are 1.51 ± 0.22 and 0.23 ± 0.08 , respectively, placing them in the upper ranges of BBA

343 hygroscopicity reported in the literature. These values are comparable to those of the aged
344 smoke in Africa (SAFARI, Magi and Hobbs, 2003) and the Yangtze River Delta background
345 station (Zhang et al., 2015a). They match the $\kappa_{f(RH)}$ of 0.22 at a rural site in southern China
346 (Kuang et al., 2021) but are lower than the values for BBA in East Asia (ACE-Asia, Kim et al.,
347 2006) and agricultural burning in INDOEX (Indian Ocean Experiment, Sheridan et al., 2002).
348 Comparing to the κ obtained from CCN measurements at a similar location in August 2017
349 ORACLES (Kacarab et al., 2020), our results are $\sim 30\%$ lower. This difference is expected
350 because κ values obtained under supersaturated conditions are typically larger than those from
351 sub-saturated conditions (Petters and Kreidenweis, 2007). This highlights the significance of
352 using the appropriate κ for sub-saturated and supersaturated investigations, such as when
353 examining aerosol liquid water content and cloud condensation nuclei activation (Rastak et al.,
354 2017; Petters and Kreidenweis, 2007).

355 Table 1. The $f(RH)$ of biomass burning aerosol from the literature.

$f(RH)$	RH	Location	Fuel type and notes	Reference
1.37	80%	Australia	light-wooded savanna fires	Gras et al., 1999
1.40	82%	northeast US	forest fires	Wang et al., 2007
1.16	80%	Brazil (SCAR-B ^a)	grass, shrub, and trees	Kotchenruther and Hobbs, 1998
1.44 ± 0.02	80%	Southern Africa (SAFARI 2000 ^b)	aged heavy smoke	Magi and Hobbs, 2003
1.60±0.20	85%	Korea (ACE-Asia ^c)	BBA	Kim et al., 2006
1.58±0.21	85%	India Ocean (INDOEX ^d)	agricultural burning	Sheridan et al., 2002
1.51±0.22	80%	South-East Atlantic Ocean (below 2 km, ORACLES)	savanna ^c	This study
1.40±0.17	80%	South-East Atlantic Ocean (above 2 km, ORACLES)	savanna ^c	This study

356

357 ^a Smoke, Clouds, and Radiation-Brazil

358 ^b Southern African Regional Science Initiative 2000

359 ^c Aerosol Characterization Experiment

360 ^d Indian Ocean Experiment

361 ^e Che et al., 2022

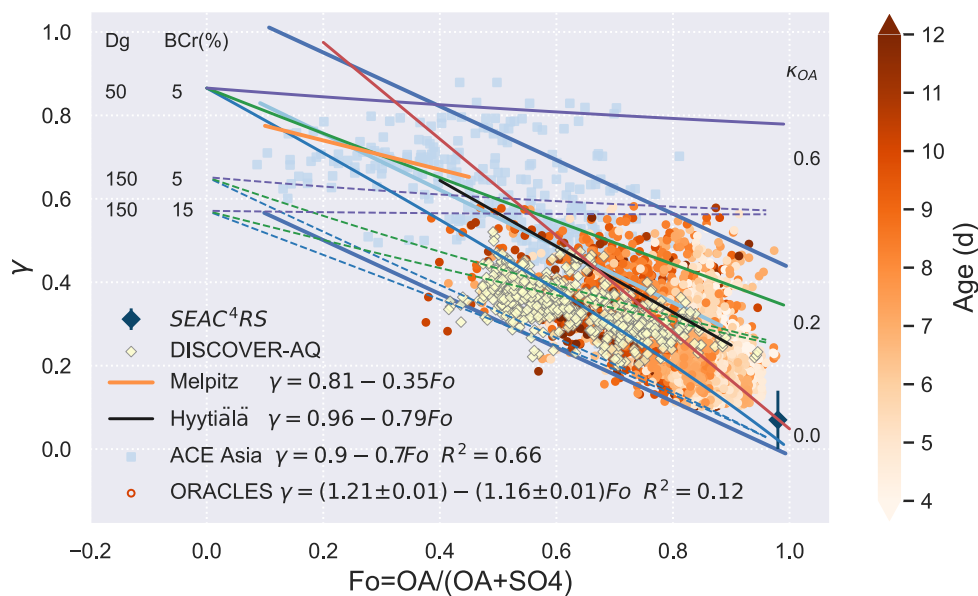
362 The mean κ_{OA} (± 1 standard deviation) is 0.11 ± 0.08 , with the 25th and 75th percentiles
363 of 0.06 and 0.16. From the vertical profiles, more hygroscopic OA are generally more aged,
364 highly oxidized, and usually located at lower altitudes (Fig. 2 and 5). In addition, we observed
365 a slight increase in κ_{OA} with volatility in 2016, with a Pearson correlation coefficient of -0.35
366 between κ_{OA} and OSc, contrasting the conventional understanding that the most volatile
367 compounds have the least hygroscopicity. This trend has been observed, albeit rarely, in field
368 and laboratory studies (e.g. Cerully et al., 2015; AsaAwuku et al., 2009). It may be related to
369 fragmentation during OA oxidation, where the highly aged and low volatile OA may dissociate
370 into more volatile fragments that are still highly functionalized and hygroscopic. However, in
371 general, no clear correlation has been found between κ_{OA} with altitude or oxidation level.

372 We noted a portion of highly aged aerosols (> 10 d) in 2016 having high OA/BC (> 12 ,
373 corresponding OA mass fraction > 50 %), in contrast to the general trend that more aged
374 aerosols correspond to smaller OA/BC (Fig. 2). About 95 % of these aerosols are above 3 km
375 and have a slightly lower f_{44} than the campaign average (Fig. S6a). Approximately 60 % belong
376 to LV-OOA with OSc > 0 and 40 % are SV-OOA (Fig. S6b). As shown in Fig. S6c, the κ_{OA}
377 values are smaller for these aerosols compared to the whole 2016 campaign, which is consistent
378 with previous studies that κ_{OA} is lower for less oxidized OA (Kuang et al., 2020; Rastak et al.,
379 2017; Mei et al., 2013); though we do not observe such correlation for the entire campaign. We
380 hypothesize that thermodynamic repartitioning has played a role, i.e. less-oxidized materials
381 condensed onto pre-existing OA under low temperature at high altitudes, resulting in smaller
382 f_{44} values and contributing to SV-OOA. These less-oxidized materials are generally less
383 functionalized and less hygroscopic, which would lead to a lower κ_{OA} .

384 3.3 Relationship with chemical composition and κ_{OA}

385

3.3.1 Comparison with various campaigns



386

387 Figure 6. γ versus F_o in various campaigns and for internally mixed OA-(NH₄)₂SO₄-BC
 388 mixtures. F_o represents the ratio of mass concentrations of OA to OA and SO₄²⁻. Solid lines in
 389 light blue and red represent the linear fits for ACE-Asia and ORACLES, respectively. Solid
 390 blue lines show the 95% prediction bands for the ACE-Asia data, in light blue rectangles, taken
 391 from Quinn et al. (2005). Colorbar represents the plume age (days) in ORACLES. Data for
 392 SEAC⁴RS is shown by dark blue diamond, taken from Shingler et al. (2016). DISCOVER-AQ
 393 data is shown by yellow diamonds, taken from NASA Langley Research Center Atmospheric
 394 Science Data Center (Atmospheric Science Data Center, 2015). Fitting lines for two European
 395 sites Melpitz (solid orange line) and Hyytiälä (solid black line) are from Zieger et al. (2015).
 396 Blue, green, and purple lines represent results for internally mixed OA-(NH₄)₂SO₄-BC
 397 mixtures with 1) a range of BC mass fraction (BCr, solid for 5% and dashed for 25%) and 2)
 398 OA with κ_{OA} of 0 (blue), 0.2 (green), and 0.6 (purple) from Mie calculations assuming a
 399 lognormal size distribution with a geometric mean diameter D_{gn} of 150 nm and a standard
 400 deviation σ_{sg} of 1.6.

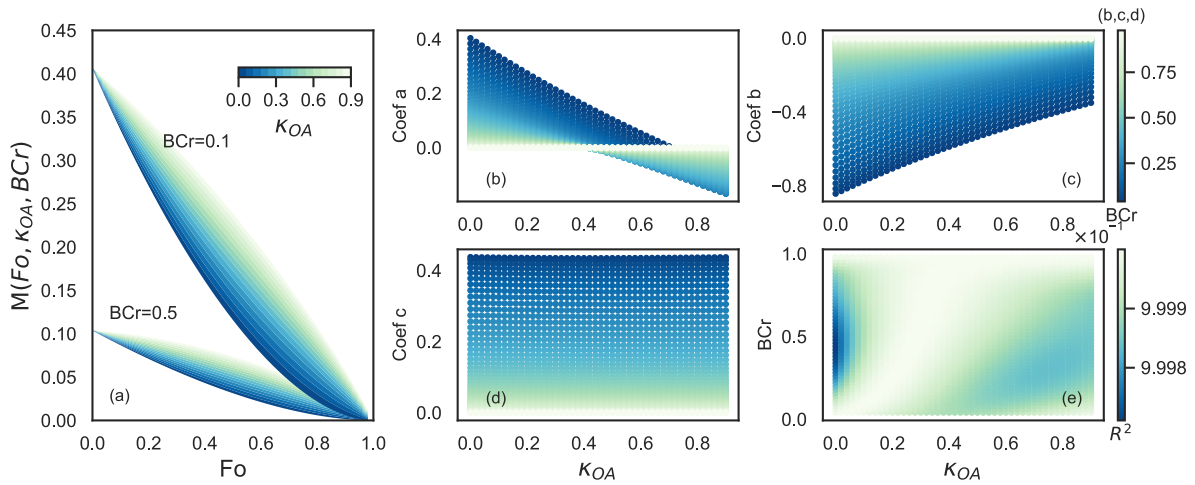
401 Quinn et al. (2005) proposed a parameterization quantifying the relationship between γ
402 and F_o , the ratio of mass concentrations of OA to OA and SO_4^{2-} , based on measurements in
403 ACE-Asia. We applied the parameterization to ORACLES measurements and as shown in Fig.
404 6, our data are well within the 95% prediction confidence intervals. We further investigated the
405 γ - F_o dependence of BBA from DISCOVER-AQ and SEAC⁴RS (Shingler et al., 2016) and
406 continental aerosols from the central European station Melpitz and a boreal site Hyytiälä in
407 Finland (Zieger et al., 2014, 2015), all showed good overlap with those from ACE-Asia and
408 ORACLES. The linear regression for ORACLES, $\gamma = (1.16 \pm 0.02) - (1.11 \pm 0.02)F_o$, retrieved
409 from an orthogonal fit by taking the standard deviation as the input for uncertainty calculation,
410 is very similar to those in Hyytiälä and ACE-Asia, though the slope is slightly lower.

411 We explored the γ - F_o relationship with the Mie model and found that the relationship
412 observed can be largely explained by aerosol chemical composition and OA hygroscopicity.
413 The γ values were calculated with the scattering coefficients simulated at both dry conditions
414 and 80 % RH were performed with Mie model for internally mixed OA-(NH₄)₂SO₄-BC
415 mixtures with assumed BC mass ratio (BCr, 5 % and 25 %), and κ_{OA} values (0-0.6), which
416 encompass the ranges observed in ORACLES (refer to Sect. 3.2 for κ_{OA} values). The PNSD
417 was assumed to be lognormally distributed, with the geometric mean diameter (D_{gn}) of 150 nm
418 and the standard deviation (σ_{sg}) of 1.6. As shown in Fig. 6 (solid and dashed purple, green, and
419 blue lines), simulated curves can capture most of the observations. F_o and κ_{OA} dominant γ , and
420 BC shows a small negative impact. It is noteworthy that the (negative) slope of the γ - F_o
421 relationship increases with increasing κ_{OA} up to κ_{OA} values of 0.6, where γ exhibits little
422 variation with F_o . Therefore, we conclude that the variation of BBA hygroscopicity with ageing
423 in the SEA is mainly due to changes in chemical composition, particularly sulphate and OA,
424 as well as the variation of OA hygroscopicity during transport. The higher BC fraction in aged
425 aerosols compared to less aged ones has slightly decreased the hygroscopicity of aged aerosols.

426

3.3.2 Parameterization of γ using Mie simulations of internally mixed OA-(NH₄)₂SO₄-

427 BC mixtures



428

429 Figure 7. (a) Variations of $M(Fo, \kappa_{OA}, BCr)$ with Fo coloured by κ_{OA} at BCr of 0.1 and 0.5,
 430 respectively, for internally mixed OA-(NH₄)₂SO₄-BC mixtures. $M(Fo, \kappa_{OA}, BCr)$ is the product
 431 of $\gamma(Fo, \kappa_{OA}=0, BCr)$ and $\gamma(Fo, \kappa_{OA}, BCr)$ for each κ_{OA} value. Fo represents the ratio of the mass
 432 concentration of OA to that of OA and SO_4^{2-} . BCr is the mass ratio of BC. (b,c,d) Variation of
 433 coefficients a, b, and c with κ_{OA} and BCr . The coefficients a, b, and c are the fitted parameters
 434 of the quadratic regression between $M(Fo, \kappa_{OA}, BCr)$ and Fo for each κ_{OA} and BCr . (e) The R^2
 435 (colorbar) of the $M(Fo, \kappa_{OA}, BCr)$ regression with Fo as a function of κ_{OA} and BCr .

436

Mie simulations are performed for internally mixed OA-(NH₄)₂SO₄-BC mixtures to
 437 obtain the scattering coefficient of dry and humidified aerosols. We assume PNSD to be a log-
 438 normal distribution with $D_{gn}=150$ nm and $\sigma_{sg} = 1.6$, as the approximation of the D_{gn} and σ_{sg} in
 439 ORACLES 2016 and 2018 campaigns. The RH and RH_{ref} is set as 80 % and 0, respectively.
 440 The γ is then calculated following Eq. 2. The Fo , κ_{OA} , and BCr are varied from 0 to 1, 0 to 0.9,
 441 and 0 to 1, respectively, all in increments of 0.02. Taking $\gamma(Fo, \kappa_{OA}=0, BCr)$ as the baseline
 442 (refer to solid and dashed blue lines in Fig. 6), we calculated the product $M(Fo, \kappa_{OA}, BCr)$ of
 443 $\gamma(Fo, \kappa_{OA}=0, BCr)$ and $\gamma(Fo, \kappa_{OA}, BCr)$ for each κ_{OA} and BCr , i.e. $M(Fo, \kappa_{OA}, BCr) =$
 444 $\gamma(Fo, \kappa_{OA}=0, BCr) * \gamma(Fo, \kappa_{OA}, BCr)$, and found that the relationship between $M(Fo, \kappa_{OA}, BCr)$ and

445 F_o can be well fitted into a quadratic (second-order) polynomial function, i.e. $M(F_o, \kappa_{OA}, BCr)$
 446 $= aF_o^2 + bF_o + c$ (Fig. 7a). The variation of $M(F_o, \kappa_{OA}, BCr)$ with F_o and the R^2 of the regression
 447 are shown in Fig. 7a and 7e, respectively. The fitted coefficients a , b , and c , as shown in Fig.
 448 7b, 7c, and 7d, coincidentally fit well as quadratic functions of κ_{OA} , whose coefficients, in turn,
 449 can be well fitted into a fifth-order polynomial function of BCr . Results are shown in Fig. S3
 450 in the supplement. In sum, the $M(F_o, \kappa_{OA}, BCr)$ can be parameterized as:

$$M(F_o, \kappa_{OA}, BCr) = \sum_{\substack{i \leq 2 \\ j \leq 2 \\ k \leq 5}} a_{ijk} BCr^k \kappa_{OA}^j F_o^i \quad (4)$$

451 Similarly, $\gamma(F_o, \kappa_{OA}=0, BCr)$ can be well fitted into a quadratic function of F_o with coefficients
 452 that fit well with a fifth-order polynomial function of BCr :

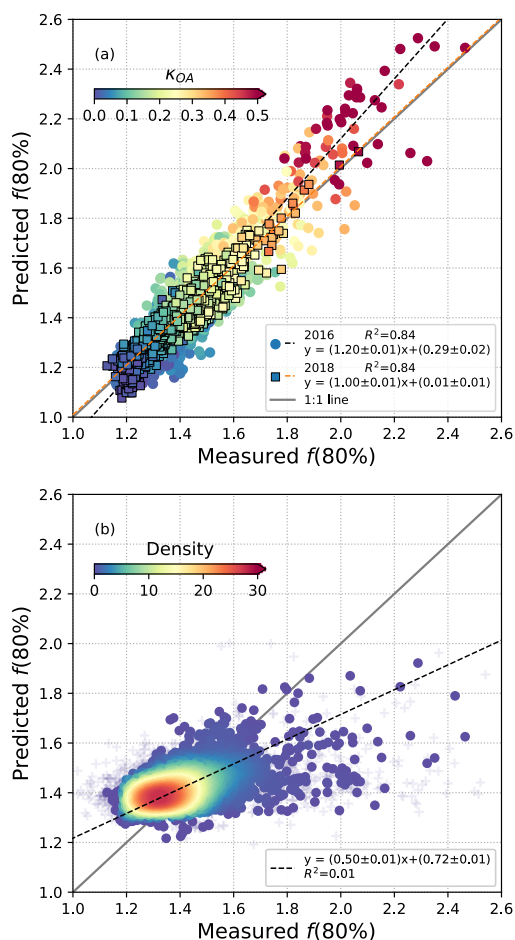
$$\gamma(F_o, \kappa_{OA} = 0, BCr) = \sum_{\substack{i \leq 2 \\ k \leq 5}} a_{ik} BCr^k F_o^i \quad (5)$$

453 Equations 4 and 5 in matrix format are referred to Eq. S1 and S2 in the supplement,
 454 respectively. Values of coefficients a_{ijk} and a_{ik} are shown in Table S3. Therefore,
 455 $\gamma(F_o, \kappa_{OA}, BCr)$ can be calculated as the ratio of $M(F_o, \kappa_{OA}, BCr)$ to $\gamma(F_o, \kappa_{OA}=0, BCr)$:

$$\gamma(F_o, \kappa_{OA}, BCr) = M(F_o, \kappa_{OA}, BCr) / \gamma(F_o, \kappa_{OA} = 0, BCr) \quad (6)$$

456 We evaluated this parameterization by comparing the predicted and measured $f(80\%)$ in
 457 ORACLES 2016 and 2018 campaigns. The predicted $f(80\%)$ is calculated with Eq. 6 with F_o ,
 458 κ_{OA} , and BCr as inputs and Eq. 2 with the dry and humidified RHs measured in both campaigns.
 459 Note the mean BC mass ratio for each year has been used in the calculation, as little difference
 460 has been observed using the temporal BCr and mean BCr . Good correlation of measured and
 461 predicted $f(80\%)$ has been achieved for both years' campaign, as shown in Fig. 8a. This
 462 indicates that the internally mixed $OA-(NH_4)_2SO_4-BC$ mixture with PNSD ($D_{gn}=150$ nm and
 463 $\sigma_{sg} = 1.6$) is a good approximation of aerosols with respect to the $f(RH)$ prediction in 2016 and

464 2018 ORACLES campaign. The influence of PNSD on $f(\text{RH})$ is small and discussed in Section
465 S1 in the supplement.



466
467 Figure 8. Measured $f(80\%)$ vs predicted $f(80\%)$ using the γ parameterization for internally
468 mixed OA-(NH₄)₂SO₄-BC mixtures. The $f(80\%)$ in subplot (a) is calculated with κ_{OA} values
469 coloured by κ_{OA} , and in subplot (b) is predicted with the mean κ_{OA} values. Black and orange
470 dashed lines in subplot (a) represent the ordinary linear regression for 2016 and 2018,
471 respectively. The black dashed line in subplot (b) represents the ordinary linear regression for
472 the two years. Grey solid line is the 1:1 line.

473 3.3.3 Sensitivity of aerosol scattering enhancement to κ_{OA}

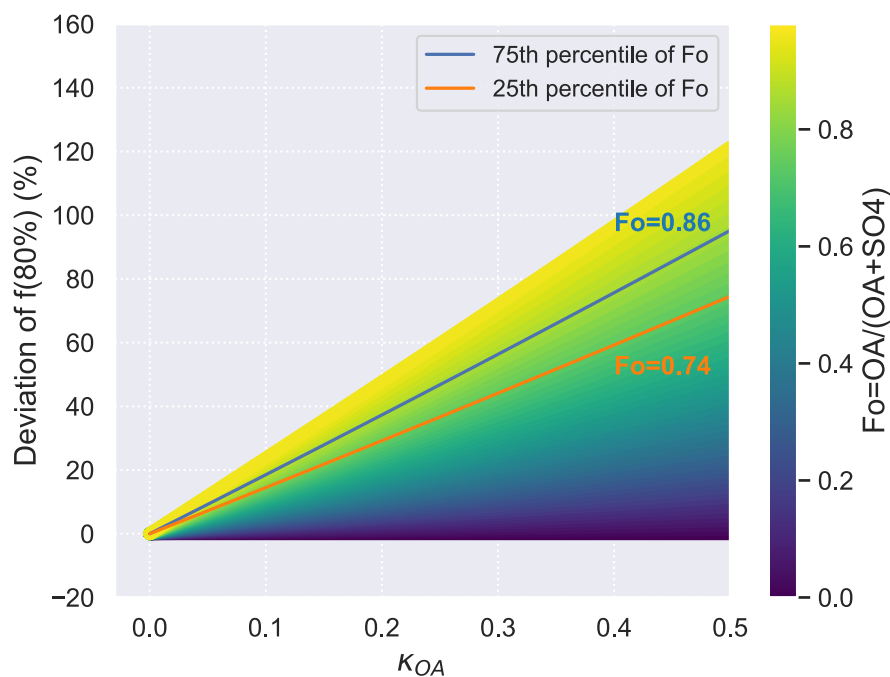
474 Due to the chemical complexity of OA, the κ_{OA} values of particles are not easily
475 obtained. Various hygroscopicity parameterizations have been proposed in previous studies,

476 most of which are parameterized with chemical composition, e.g. organics or inorganics
477 fraction, and a constant assumed κ_{OA} value. Few studies consider the variation of κ_{OA} (Zhang
478 et al., 2015b; Huang et al., 2022). While these parameterizations can represent their
479 observations well, they may not be suitable for situations with different κ_{OA} values. Therefore,
480 in this section, the influence of κ_{OA} on the prediction of $f(\text{RH})$ is analyzed. We calculated the
481 $f(80\%)$ with the mean κ_{OA} in each campaign and the results are shown in Fig. 8b. The use of a
482 constant κ_{OA} average leads to a much smaller variation of the predicted $f(80\%)$ values, with
483 most of which concentrated around 1.3-1.4. Predicted $f(80\%)$ tend to overestimate lower
484 $f(80\%)$ values while underestimate higher $f(80\%)$ values. A slope of 0.50 and a R^2 of 0.01
485 indicates poor prediction in capturing the trend of $f(80\%)$. This indicates that using Fo, BCr,
486 and a constant κ_{OA} is insufficient for the prediction of $f(\text{RH})$, and that the variation of κ_{OA} need
487 to be considered, at least for situations where κ_{OA} has a large variation, such as in ORACLES.

488 To quantitatively investigate the sensitivity of $f(\text{RH})$ to κ_{OA} , we calculated the deviation
489 of $f(80\%)$ with κ_{OA} for the OA-(NH₄)₂SO₄-BC mixture. The deviation of $f(80\%)$ was calculated
490 as $f(80\%, \kappa_{\text{OA}}) - f(80\%, \kappa_{\text{OA}}=0)$. As shown in Fig. 9, we observed that κ_{OA} is positively correlated
491 with $f(80\%)$. Additionally, the deviation of $f(80\%)$ is dependent on the OA fraction (Fo), i.e. a
492 higher OA fraction leads to a larger impact of κ_{OA} and consequently a larger deviation of
493 $f(80\%)$.

494 The 25th and 75th percentiles of Fo in 2016 and 2018 ORACLES campaign were 0.74
495 and 0.86, respectively. These are relatively high values and therefore result in relatively high
496 spread of $f(80\%)$. Additionally, the age of ORACLES OA spans from <4 days to > 10 days,
497 during which OA oxidation and fragmentation (as discussed in Section 3.2) takes place. These
498 processes alter the hygroscopicity of OA, causing the OA in ORACLES to contribute to large
499 variations of κ_{OA} . These large variations of κ_{OA} , combined with the relatively high OA fraction
500 (Fo), makes $f(\text{RH})$ highly sensitive to the κ_{OA} value. For aerosols with a κ_{OA} of 0.4 and a Fo of

501 0.86, the $f(80\%)$ can be 80 % higher compared to aerosols with hydrophobic OA, as shown in
 502 Fig. 9. In other words, the aerosol scattering coefficients at 80 % RH are 80 % higher solely
 503 because of the increase of OA hygroscopicity. This high sensitivity also explains the poor
 504 prediction of $f(80\%)$ when using campaign mean κ_{OA} values, as shown in Fig. 8b. Many studies
 505 overlook the variability of κ_{OA} and instead use a constant κ_{OA} when analyzing aerosol
 506 hygroscopicity or radiative forcing. As illustrated in Fig. 9, this can be reasonable when the
 507 OA fraction is low and κ_{OA} exhibits minimal variation; however, in cases where these two
 508 conditions are not met, κ_{OA} can significantly influence the scattering coefficients and hence
 509 direct radiative forcing.



510

511 Figure 9. Sensitivity of the deviation of $f(80\%)$ to κ_{OA} . The deviation of $f(80\%)$ was calculated
 512 as $f(80\%, \kappa_{OA}) - f(80\%, \kappa_{OA}=0)$. The OA to OA + SO₄ ratio (Fo) is represented by the colorbar.
 513 The blue and orange lines represent the variation at 75th and 25th percentile of Fo in both years'
 514 ORACLES campaign, respectively.

515 **4 Conclusion**

516 The hygroscopicity of aerosols from the perspective of scattering enhancement over the
517 SEA Ocean during the BB season are investigated using measurements from the 2016 and 2018
518 ORACLES campaigns. The vertical distribution of aerosol hygroscopicity shows a consistent
519 pattern in both campaigns, remaining stable above 2 km; below 2 km, aerosols are more
520 hygroscopic at lower altitudes. Aerosols above 2 km have a mean and standard deviation of
521 $f(80\%)$ and $\kappa_{f(RH)}$ of 1.40 ± 0.17 and 0.19 ± 0.07 , respectively, and are less hygroscopic.
522 Conversely, aerosols below 2 km are more hygroscopic, and have a mean and standard
523 deviation of $f(80\%)$ and $\kappa_{f(RH)}$ of 1.51 ± 0.22 and 0.23 ± 0.08 , respectively, which are values at
524 the upper level of BBA hygroscopicity found in the literature. This variation of aerosol
525 hygroscopicity is consistent with the vertical variation of chemical composition. The OA and
526 sulphate mass fraction in both years show little variation above 2 km; while below this altitude,
527 OA decreases with decreasing altitude, while the sulphate mass fraction tends to increase. OA
528 oxidation through molecular fragmentation is the main mechanism for OA losses in the FT.
529 While the increase of sulphate in the MBL could indicate marine influence.

530 We retrieved κ_{OA} using Mie simulations. It shows a large variation, with the mean and
531 standard deviation being 0.11 ± 0.08 and the 25th and 75th percentiles of 0.06 and 0.16,
532 respectively. No clear relationship was found between κ_{OA} and OA oxidation level; while a
533 slight increase in κ_{OA} with volatility is shown in 2016, which may be related to the
534 fragmentation during OA oxidation, where the highly aged and low volatile OA may dissociate
535 into more volatile fragments that are still highly functionalized and hygroscopic. In all, OA
536 hygroscopicity under sub-saturated conditions can be largely influenced by solubility,
537 molecular weight, molecular functional groups, and carbon number (Cai et al., 2021; Kuang et
538 al., 2020; Rastak et al., 2017; Rickards et al., 2013; Suda et al., 2012); to better understand the
539 variation of κ_{OA} , more molecular investigations are needed.

540 In comparison with other campaigns, we find the variation of aerosol hygroscopicity in
541 the SEA is mainly due to changes in chemical composition, particularly sulphate and OA, as
542 well as variations in OA hygroscopicity during transport. To quantitatively investigate this
543 relationship, we came up with a parameterization using F_o , BC_r , and κ_{OA} , and the $f(80\%)$ from
544 Mie simulations for internally mixed OA-(NH₄)₂SO₄-BC mixture with PNSD ($D_{gn}=150$ nm
545 and $\sigma_{sg}=1.6$). This suggests that the internal mixture of OA-(NH₄)₂SO₄-BC is a good
546 approximation of aerosols with respect to the $f(RH)$ prediction in 2016 and 2018 ORACLES
547 campaign.

548 A sensitivity study indicates that solely due to the increase in OA hygroscopicity
549 observed in our study, the aerosol scattering coefficients at 80 % RH can be amplified by 80 %.
550 Relying on the campaign's mean κ_{OA} value leads to a poor prediction of $f(80\%)$. The
551 dependence of $f(RH)$ on κ_{OA} suggests that using a constant κ_{OA} can be acceptable when the OA
552 fraction is low and κ_{OA} demonstrates limited variations. However, in situations where these
553 two conditions are not met, κ_{OA} can significantly influence the scattering coefficients and thus
554 aerosol radiative effect. Therefore, accommodating the variability of κ_{OA} is advisable.

555

556 *Competing interests.* At least one of the (co-)authors is a guest member of the editorial board
557 of Atmospheric Chemistry and Physics for the special issue “New observations and related
558 modelling studies of the aerosol-cloud-climate system in the Southeast Atlantic and southern
559 Africa regions”. The authors have no other competing interests to declare.

560

561 *Special issue statement.* This article is part of the special issue “New observations and related
562 modeling studies of the aerosol-cloud-climate system in the Southeast Atlantic and southern
563 Africa regions (ACP/AMT inter-journal SI)”. It is not associated with a conference.

564

565 *Data Availability.* Data sets are publicly available via the digital object identifier provided
566 under ORACLES Science Team reference:
567 https://doi.org/10.5067/Suborbital/ORACLES/P3/2018_V2.

568

569 *Acknowledgments.* The authors would like to thank the ORACLES team. Lu Zhang thanks the
570 postdoctoral fellowship funding from Tel Aviv University, Department of Exact Sciences.
571 Michal Segal-Rozenhaimer and Haochi Che were supported by United States Department of
572 Energy Atmospheric System Research (ASR) grant DE-SC0020084. Caroline Dang thanks the
573 NASA Postdoctoral Fellowship Grant. Paola Formenti is supported by the AEROSOLS, RADIATION
574 and CLOUDS in southern Africa (AEROCLO-SA) project funded by the French National
575 Research Agency under grant agreement n° ANR-15-CE01-0014-01, the French national
576 programs LEFE/INSU and PNTS, the French National Agency for Space Studies (CNES), the
577 European Union's 7th Framework Programme (FP7/2014-2018) under EUFAR2 contract
578 n°312609, and the South African National Research Foundation (NRF) under grant UID
579 105958. The authors thank Paul Zieger for useful comments on this article.

580

581 *Financial support.* This research has been supported by the Tel Aviv University (postdoctoral
582 fellowship); the United States Department of Energy (DOE) Atmospheric System Research
583 (ASR; grant DE-SC0020084); a NASA postdoctoral fellowship; the AEROSOLS, RADIATION and
584 CLOUDS in southern Africa (AEROCLO-SA) project funded by the French National Research
585 Agency (grant agreement no. ANR-15-CE01-0014-01); the French national programs
586 LEFE/INSU and PNTS; the French National Agency for Space Studies (CNES); the European
587 Union's Seventh Framework Programme (FP7/2014-2018; EUFAR2 contract no. 312609); and
588 the South African National Research Foundation (NRF; grant UID 105958).

589

590

591 **References**

- 592 Alexander, B., Park, R. J., Jacob, D. J., Li, Q. B., Yantosca, R. M., Savarino, J., Lee, C. C.
593 W., and Thiemens, M. H.: Sulfate formation in sea-salt aerosols: Constraints from oxygen
594 isotopes, *J. Geophys. Res. Atmospheres*, 110, <https://doi.org/10.1029/2004JD005659>, 2005.
- 595 Andreae, M. O., Elbert, W., and de Mora, S. J.: Biogenic sulfur emissions and aerosols over
596 the tropical South Atlantic: 3. Atmospheric dimethylsulfide, aerosols and cloud condensation
597 nuclei, *J. Geophys. Res. Atmospheres*, 100, 11335–11356,
598 <https://doi.org/10.1029/94JD02828>, 1995.
- 599 Bukowiecki, N., Weingartner, E., Gysel, M., Coen, M. C., Zieger, P., Herrmann, E.,
600 Steinbacher, M., Gäggeler, H. W., and Baltensperger, U.: A Review of More than 20 Years
601 of Aerosol Observation at the High Altitude Research Station Jungfraujoch, Switzerland
602 (3580 m asl), *Aerosol Air Qual. Res.*, 16, 764–788,
603 <https://doi.org/10.4209/aaqr.2015.05.0305>, 2016.
- 604 Burgos, M. A., Andrews, E., Titos, G., Benedetti, A., Bian, H., Buchard, V., Curci, G.,
605 Kipling, Z., Kirkevåg, A., Kokkola, H., Laakso, A., Letertre-Danczak, J., Lund, M. T.,
606 Matsui, H., Myhre, G., Randles, C., Schulz, M., van Noije, T., Zhang, K., Alados-Arboledas,
607 L., Baltensperger, U., Jefferson, A., Sherman, J., Sun, J., Weingartner, E., and Zieger, P.: A
608 global model–measurement evaluation of particle light scattering coefficients at elevated
609 relative humidity, *Atmospheric Chem. Phys.*, 20, 10231–10258, [https://doi.org/10.5194/acp-](https://doi.org/10.5194/acp-20-10231-2020)
610 [20-10231-2020](https://doi.org/10.5194/acp-20-10231-2020), 2020.
- 611 Cai, M., Liang, B., Sun, Q., Liu, L., Yuan, B., Shao, M., Huang, S., Peng, Y., Wang, Z., Tan,
612 H., Li, F., Xu, H., Chen, D., and Zhao, J.: The important roles of surface tension and growth
613 rate in the contribution of new particle formation (NPF) to cloud condensation nuclei (CCN)
614 number concentration: evidence from field measurements in southern China, *Atmospheric*
615 *Chem. Phys.*, 21, 8575–8592, <https://doi.org/10.5194/acp-21-8575-2021>, 2021.
- 616 Carrico, C. M., Kus, P., Rood, M. J., Quinn, P. K., and Bates, T. S.: Mixtures of pollution,
617 dust, sea salt, and volcanic aerosol during ACE-Asia: Radiative properties as a function of
618 relative humidity, *J. Geophys. Res. Atmospheres*, 108,
619 <https://doi.org/10.1029/2003JD003405>, 2003.
- 620 Cerully, K. M., Bougiatioti, A., Hite, J. R. J., Guo, H., Xu, L., Ng, N. L., Weber, R., and
621 Nenes, A.: On the link between hygroscopicity, volatility, and oxidation state of ambient and
622 water-soluble aerosols in the southeastern United States, *Atmospheric Chem. Phys.*, 15,
623 8679–8694, <https://doi.org/10.5194/acp-15-8679-2015>, 2015.
- 624 Che, H., Zhang, X., Zhang, L., Wang, Y., Zhang, Y., Shen, X., Ma, Q., Sun, J., and Zhong, J.:
625 Prediction of size-resolved number concentration of cloud condensation nuclei and long-term
626 measurements of their activation characteristics, *Sci. Rep.*, 7, 5819,
627 <https://doi.org/10.1038/s41598-017-05998-3>, 2017.

- 628 Che, H., Segal-Rozenhaimer, M., Zhang, L., and Dang, C.: Transport and aging of biomass
629 burning aerosols in the South-eastern Atlantic Ocean, *Commun. Earth Environ.*, Accepted,
630 2021.
- 631 Che, H., Segal-Rozenhaimer, M., Zhang, L., Dang, C., Zuidema, P., Dobracki, A., Sedlacek,
632 A. J., Coe, H., Wu, H., Taylor, J., Zhang, X., Redemann, J., and Haywood, J.: Cloud
633 processing and weeklong ageing affect biomass burning aerosol properties over the south-
634 eastern Atlantic, *Commun. Earth Environ.*, 3, 182, <https://doi.org/10.1038/s43247-022-00517-3>, 2022a.
- 636 Che, H., Stier, P., Watson-Parris, D., Gordon, H., and Deaconu, L.: Source attribution of
637 cloud condensation nuclei and their impact on stratocumulus clouds and radiation in the
638 south-eastern Atlantic, *Atmospheric Chem. Phys. Discuss.*, 1–26, <https://doi.org/10.5194/acp-2022-43>, 2022b.
- 640 Chen, J., Zhao, C. S., Ma, N., and Yan, P.: Aerosol hygroscopicity parameter derived from
641 the light scattering enhancement factor measurements in the North China Plain, *Atmospheric
642 Chem. Phys.*, 14, 8105–8118, <https://doi.org/10.5194/acp-14-8105-2014>, 2014.
- 643 Cotterell, M. I., Willoughby, R. E., Bzdek, B. R., Orr-Ewing, A. J., and Reid, J. P.: A
644 complete parameterisation of the relative humidity and wavelength dependence of the
645 refractive index of hygroscopic inorganic aerosol particles, *Atmospheric Chem. Phys.*, 17,
646 9837–9851, <https://doi.org/10.5194/acp-17-9837-2017>, 2017.
- 647 Covert, D. S., Charlson, R. J., and Ahlquist, N. C.: A Study of the Relationship of Chemical
648 Composition and Humidity to Light Scattering by Aerosols, *J. Appl. Meteorol.*, 11, 968–976,
649 [https://doi.org/10.1175/1520-0450\(1972\)011<0968:ASOTRO>2.0.CO;2](https://doi.org/10.1175/1520-0450(1972)011<0968:ASOTRO>2.0.CO;2), 1972.
- 650 Cubison, M. J., Ortega, A. M., Hayes, P. L., Farmer, D. K., Day, D., Lechner, M. J., Brune,
651 W. H., Apel, E., Diskin, G. S., Fisher, J. A., Fuelberg, H. E., Hecobian, A., Knapp, D. J.,
652 Mikoviny, T., Riemer, D., Sachse, G. W., Sessions, W., Weber, R. J., Weinheimer, A. J.,
653 Wisthaler, A., and Jimenez, J. L.: Effects of aging on organic aerosol from open biomass
654 burning smoke in aircraft and laboratory studies, *Atmospheric Chem. Phys.*, 11, 12049–
655 12064, <https://doi.org/10.5194/acp-11-12049-2011>, 2011.
- 656 Day, D. E., Hand, J. L., Carrico, C. M., Engling, G., and Malm, W. C.: Humidification
657 factors from laboratory studies of fresh smoke from biomass fuels, *J. Geophys. Res.
658 Atmospheres*, 111, <https://doi.org/10.1029/2006JD007221>, 2006.
- 659 DeCarlo, P. F., Slowik, J. G., Worsnop, D. R., Davidovits, P., and Jimenez, J. L.: Particle
660 Morphology and Density Characterization by Combined Mobility and Aerodynamic
661 Diameter Measurements. Part 1: Theory, *Aerosol Sci. Technol.*, 38, 1185–1205,
662 <https://doi.org/10.1080/027868290903907>, 2004.
- 663 Ervens, B., Cubison, M., Andrews, E., Feingold, G., Ogren, J. A., Jimenez, J. L., DeCarlo, P.,
664 and Nenes, A.: Prediction of cloud condensation nucleus number concentration using
665 measurements of aerosol size distributions and composition and light scattering enhancement
666 due to humidity, *J. Geophys. Res. Atmospheres*, 112, <https://doi.org/10.1029/2006JD007426>,
667 2007.

668 Gras, J. L., Jensen, J. B., Okada, K., Ikegami, M., Zaizen, Y., and Makino, Y.: Some optical
669 properties of smoke aerosol in Indonesia and tropical Australia, *Geophys. Res. Lett.*, 26,
670 1393–1396, <https://doi.org/10.1029/1999GL900275>, 1999.

671 Gysel, M., Crosier, J., Topping, D. O., Whitehead, J. D., Bower, K. N., Cubison, M. J.,
672 Williams, P. I., Flynn, M. J., McFiggans, G. B., and Coe, H.: Closure study between chemical
673 composition and hygroscopic growth of aerosol particles during TORCH2, *Atmospheric*
674 *Chem. Phys.*, 7, 6131–6144, <https://doi.org/10.5194/acp-7-6131-2007>, 2007.

675 Haywood, J., Bush, M., Abel, S., Claxton, B., Coe, H., Crosier, J., Harrison, M., Macpherson,
676 B., Naylor, M., and Osborne, S.: Prediction of visibility and aerosol within the operational
677 Met Office Unified Model. II: Validation of model performance using observational data, *Q.*
678 *J. R. Meteorol. Soc.*, 134, 1817–1832, <https://doi.org/10.1002/qj.275>, 2008.

679 Howell, S. G., Freitag, S., Dobracki, A., Smirnow, N., and Sedlacek III, A. J.: Undersizing of
680 aged African biomass burning aerosol by an ultra-high-sensitivity aerosol spectrometer,
681 *Atmospheric Meas. Tech.*, 14, 7381–7404, <https://doi.org/10.5194/amt-14-7381-2021>, 2021.

682 Huang, S., Wu, Z., Wang, Y., Poulain, L., Höpner, F., Merkel, M., Herrmann, H., and
683 Wiedensohler, A.: Aerosol Hygroscopicity and its Link to Chemical Composition in a
684 Remote Marine Environment Based on Three Transatlantic Measurements, *Environ. Sci.*
685 *Technol.*, <https://doi.org/10.1021/acs.est.2c00785>, 2022.

686 Kacarab, M., Thornhill, K. L., Dobracki, A., Howell, S. G., O'Brien, J. R., Freitag, S.,
687 Poellot, M. R., Wood, R., Zuidema, P., Redemann, J., and Nenes, A.: Biomass burning
688 aerosol as a modulator of the droplet number in the southeast Atlantic region, *Atmospheric*
689 *Chem. Phys.*, 20, 3029–3040, <https://doi.org/10.5194/acp-20-3029-2020>, 2020.

690 Kim, J., Yoon, S.-C., Jefferson, A., and Kim, S.-W.: Aerosol hygroscopic properties during
691 Asian dust, pollution, and biomass burning episodes at Gosan, Korea in April 2001, *Atmos.*
692 *Environ.*, 40, 1550–1560, <https://doi.org/10.1016/j.atmosenv.2005.10.044>, 2006.

693 Klopper, D., Formenti, P., Namwoonde, A., Cazaunau, M., Chevaillier, S., Feron, A.,
694 Gaimoz, C., Hease, P., Lahmidi, F., Mirande-Bret, C., Triquet, S., Zeng, Z., and Piketh, S. J.:
695 Chemical composition and source apportionment of atmospheric aerosols on the Namibian
696 coast, *Atmospheric Chem. Phys.*, 20, 15811–15833, [https://doi.org/10.5194/acp-20-15811-](https://doi.org/10.5194/acp-20-15811-2020)
697 2020, 2020.

698 Kotchenruther, R. A. and Hobbs, P. V.: Humidification factors of aerosols from biomass
699 burning in Brazil, *J. Geophys. Res. Atmospheres*, 103, 32081–32089,
700 <https://doi.org/10.1029/98JD00340>, 1998.

701 Kuang, Y., Xu, W., Tao, J., Ma, N., Zhao, C., and Shao, M.: A Review on Laboratory Studies
702 and Field Measurements of Atmospheric Organic Aerosol Hygroscopicity and Its
703 Parameterization Based on Oxidation Levels, *Curr. Pollut. Rep.*, 6, 410–424,
704 <https://doi.org/10.1007/s40726-020-00164-2>, 2020.

705 Kuang, Y., Huang, S., Xue, B., Luo, B., Song, Q., Chen, W., Hu, W., Li, W., Zhao, P., Cai,
706 M., Peng, Y., Qi, J., Li, T., Wang, S., Chen, D., Yue, D., Yuan, B., and Shao, M.: Contrasting
707 effects of secondary organic aerosol formations on organic aerosol hygroscopicity,

708 Atmospheric Chem. Phys., 21, 10375–10391, <https://doi.org/10.5194/acp-21-10375-2021>,
709 2021.

710 Lambe, A. T., Onasch, T. B., Massoli, P., Croasdale, D. R., Wright, J. P., Ahern, A. T.,
711 Williams, L. R., Worsnop, D. R., Brune, W. H., and Davidovits, P.: Laboratory studies of the
712 chemical composition and cloud condensation nuclei (CCN) activity of secondary organic
713 aerosol (SOA) and oxidized primary organic aerosol (OPOA), *Atmospheric Chem. Phys.*, 11,
714 8913–8928, <https://doi.org/10.5194/acp-11-8913-2011>, 2011.

715 Liu, P., Song, M., Zhao, T., Gunthe, S. S., Ham, S., He, Y., Qin, Y. M., Gong, Z., Amorim, J.
716 C., Bertram, A. K., and Martin, S. T.: Resolving the mechanisms of hygroscopic growth and
717 cloud condensation nuclei activity for organic particulate matter, *Nat. Commun.*, 9, 1–10,
718 <https://doi.org/10.1038/s41467-018-06622-2>, 2018.

719 Liu, P. F., Zhao, C. S., Göbel, T., Hallbauer, E., Nowak, A., Ran, L., Xu, W. Y., Deng, Z. Z.,
720 Ma, N., Mildenerger, K., Henning, S., Stratmann, F., and Wiedensohler, A.: Hygroscopic
721 properties of aerosol particles at high relative humidity and their diurnal variations in the
722 North China Plain, *Atmospheric Chem. Phys.*, 11, 3479–3494, [https://doi.org/10.5194/acp-](https://doi.org/10.5194/acp-11-3479-2011)
723 11-3479-2011, 2011.

724 Liu, X. and Wang, J.: How important is organic aerosol hygroscopicity to aerosol indirect
725 forcing?, *Environ. Res. Lett.*, 5, 044010, <https://doi.org/10.1088/1748-9326/5/4/044010>,
726 2010.

727 Magi, B. I. and Hobbs, P. V.: Effects of humidity on aerosols in southern Africa during the
728 biomass burning season, *J. Geophys. Res. Atmospheres*, 108,
729 <https://doi.org/10.1029/2002JD002144>, 2003.

730 Mayer, K. J., Wang, X., Santander, M. V., Mitts, B. A., Sauer, J. S., Sultana, C. M., Cappa,
731 C. D., and Prather, K. A.: Secondary Marine Aerosol Plays a Dominant Role over Primary
732 Sea Spray Aerosol in Cloud Formation, *ACS Cent. Sci.*, 6, 2259–2266,
733 <https://doi.org/10.1021/acscentsci.0c00793>, 2020.

734 Mei, F., Hayes, P. L., Ortega, A., Taylor, J. W., Allan, J. D., Gilman, J., Kuster, W., de
735 Gouw, J., Jimenez, J. L., and Wang, J.: Droplet activation properties of organic aerosols
736 observed at an urban site during CalNex-LA, *J. Geophys. Res. Atmospheres*, 118, 2903–
737 2917, <https://doi.org/10.1002/jgrd.50285>, 2013.

738 Mie, G.: Beiträge zur Optik trüber Medien, speziell kolloidaler Metallösungen, *Ann. Phys.*,
739 330, 377–445, <https://doi.org/10.1002/andp.19083300302>, 1908.

740 Petters, M. D. and Kreidenweis, S. M.: A single parameter representation of hygroscopic
741 growth and cloud condensation nucleus activity, *Atmos Chem Phys*, 11, 2007.

742 Petters, M. D., Carrico, C. M., Kreidenweis, S. M., Prenni, A. J., DeMott, P. J., Collett, J. L.,
743 and Moosmüller, H.: Cloud condensation nucleation activity of biomass burning aerosol, *J.*
744 *Geophys. Res.*, 114, D22205, <https://doi.org/10.1029/2009JD012353>, 2009.

745 Quinn, P. K., Bates, T. S., Baynard, T., Clarke, A. D., Onasch, T. B., Wang, W., Rood, M. J.,
746 Andrews, E., Allan, J., Carrico, C. M., Coffman, D., and Worsnop, D.: Impact of particulate
747 organic matter on the relative humidity dependence of light scattering: A simplified
748 parameterization, *Geophys. Res. Lett.*, 32, <https://doi.org/10.1029/2005GL024322>, 2005.

749 Rastak, N., Pajunoja, A., Acosta Navarro, J. C., Ma, J., Song, M., Partridge, D. G., Kirkevåg,
750 A., Leong, Y., Hu, W. W., Taylor, N. F., Lambe, A., Cerully, K., Bougiatioti, A., Liu, P.,
751 Krejci, R., Petäjä, T., Percival, C., Davidovits, P., Worsnop, D. R., Ekman, A. M. L., Nenes,
752 A., Martin, S., Jimenez, J. L., Collins, D. R., Topping, D. o., Bertram, A. K., Zuend, A.,
753 Virtanen, A., and Riipinen, I.: Microphysical explanation of the RH-dependent water affinity
754 of biogenic organic aerosol and its importance for climate, *Geophys. Res. Lett.*, 44, 5167–
755 5177, <https://doi.org/10.1002/2017GL073056>, 2017.

756 Reddington, C. L., Morgan, W. T., Darbyshire, E., Brito, J., Coe, H., Artaxo, P., Scott, C. E.,
757 Marsham, J., and Spracklen, D. V.: Biomass burning aerosol over the Amazon: analysis of
758 aircraft, surface and satellite observations using a global aerosol model, *Atmospheric Chem.*
759 *Phys.*, 19, 9125–9152, <https://doi.org/10.5194/acp-19-9125-2019>, 2019.

760 Redemann, J., Wood, R., Zuidema, P., Doherty, S. J., Luna, B., LeBlanc, S. E., Diamond, M.
761 S., Shinozuka, Y., Chang, I. Y., Ueyama, R., Pfister, L., Ryoo, J.-M., Dobracki, A. N., da
762 Silva, A. M., Longo, K. M., Kacenelenbogen, M. S., Flynn, C. J., Pistone, K., Knox, N. M.,
763 Piketh, S. J., Haywood, J. M., Formenti, P., Mallet, M., Stier, P., Ackerman, A. S., Bauer, S.
764 E., Fridlind, A. M., Carmichael, G. R., Saide, P. E., Ferrada, G. A., Howell, S. G., Freitag, S.,
765 Cairns, B., Holben, B. N., Knobelspiesse, K. D., Tanelli, S., L’Ecuyer, T. S., Dzambo, A. M.,
766 Sy, O. O., McFarquhar, G. M., Poellot, M. R., Gupta, S., O’Brien, J. R., Nenes, A., Kacarab,
767 M., Wong, J. P. S., Small-Griswold, J. D., Thornhill, K. L., Noone, D., Podolske, J. R.,
768 Schmidt, K. S., Pilewskie, P., Chen, H., Cochrane, S. P., Sedlacek, A. J., Lang, T. J., Stith,
769 E., Segal-Rozenhaimer, M., Ferrare, R. A., Burton, S. P., Hostetler, C. A., Diner, D. J.,
770 Seidel, F. C., Platnick, S. E., Myers, J. S., Meyer, K. G., Spangenberg, D. A., Maring, H., and
771 Gao, L.: An overview of the ORACLES (ObseRvations of Aerosols above CLouds and their
772 intEractionS) project: aerosol–cloud–radiation interactions in the southeast Atlantic basin,
773 *Atmospheric Chem. Phys.*, 21, 1507–1563, <https://doi.org/10.5194/acp-21-1507-2021>, 2021.

774 Rickards, A. M. J., Miles, R. E. H., Davies, J. F., Marshall, F. H., and Reid, J. P.:
775 Measurements of the Sensitivity of Aerosol Hygroscopicity and the κ Parameter to the O/C
776 Ratio, *J. Phys. Chem. A*, 117, 14120–14131, <https://doi.org/10.1021/jp407991n>, 2013.

777 Sheridan, P. J., Jefferson, A., and Ogren, J. A.: Spatial variability of submicrometer aerosol
778 radiative properties over the Indian Ocean during INDOEX, *J. Geophys. Res. Atmospheres*,
779 107, <https://doi.org/10.1029/2000JD000166>, 2002.

780 Shingler, T., Crosbie, E., Ortega, A., Shiraiwa, M., Zuend, A., Beyersdorf, A., Ziemba, L.,
781 Anderson, B., Thornhill, L., Perring, A. E., Schwarz, J. P., Campazano-Jost, P., Day, D. A.,
782 Jimenez, J. L., Hair, J. W., Mikoviny, T., Wisthaler, A., and Sorooshian, A.: Airborne
783 characterization of subsaturated aerosol hygroscopicity and dry refractive index from the
784 surface to 6.5 km during the SEAC4RS campaign, *J. Geophys. Res. Atmospheres*, 121,
785 4188–4210, <https://doi.org/10.1002/2015JD024498>, 2016.

786 Suda, S. R., Petters, M. D., Matsunaga, A., Sullivan, R. C., Ziemann, P. J., and Kreidenweis,
787 S. M.: Hygroscopicity frequency distributions of secondary organic aerosols, *J. Geophys.*
788 *Res. Atmospheres*, 117, <https://doi.org/10.1029/2011JD016823>, 2012.

789 Sumlin, B. J., Heinson, Y. W., Shetty, N., Pandey, A., Pattison, R. S., Baker, S., Hao, W. M.,
790 and Chakrabarty, R. K.: UV–Vis–IR spectral complex refractive indices and optical
791 properties of brown carbon aerosol from biomass burning, *J. Quant. Spectrosc. Radiat.*
792 *Transf.*, 206, 392–398, <https://doi.org/10.1016/j.jqsrt.2017.12.009>, 2018.

- 793 Thompson, G. and Eidhammer, T.: A Study of Aerosol Impacts on Clouds and Precipitation
794 Development in a Large Winter Cyclone, *J. Atmospheric Sci.*, 71, 3636–3658,
795 <https://doi.org/10.1175/JAS-D-13-0305.1>, 2014.
- 796 Titos, G., Cazorla, A., Zieger, P., Andrews, E., Lyamani, H., Granados-Muñoz, M. J., Olmo,
797 F. J., and Alados-Arboledas, L.: Effect of hygroscopic growth on the aerosol light-scattering
798 coefficient: A review of measurements, techniques and error sources, *Atmos. Environ.*, 141,
799 494–507, <https://doi.org/10.1016/j.atmosenv.2016.07.021>, 2016.
- 800 Titos, G., Burgos, M. A., Zieger, P., Alados-Arboledas, L., Baltensperger, U., Jefferson, A.,
801 Sherman, J., Weingartner, E., Henzing, B., Luoma, K., O’Dowd, C., Wiedensohler, A., and
802 Andrews, E.: A global study of hygroscopicity-driven light-scattering enhancement in the
803 context of other in situ aerosol optical properties, *Atmospheric Chem. Phys.*, 21, 13031–
804 13050, <https://doi.org/10.5194/acp-21-13031-2021>, 2021.
- 805 Wang, J., Shilling, J. E., Liu, J., Zelenyuk, A., Bell, D. M., Petters, M. D., Thalman, R., Mei,
806 F., Zaveri, R. A., and Zheng, G.: Cloud droplet activation of secondary organic aerosol is
807 mainly controlled by molecular weight, not water solubility, *Atmospheric Chem. Phys.*, 19,
808 941–954, <https://doi.org/10.5194/acp-19-941-2019>, 2019.
- 809 Wang, W., Rood, M. J., Carrico, C. M., Covert, D. S., Quinn, P. K., and Bates, T. S.: Aerosol
810 optical properties along the northeast coast of North America during the New England Air
811 Quality Study–Intercontinental Transport and Chemical Transformation 2004 campaign and
812 the influence of aerosol composition, *J. Geophys. Res. Atmospheres*, 112,
813 <https://doi.org/10.1029/2006JD007579>, 2007.
- 814 van der Werf, G. R., Randerson, J. T., Giglio, L., Collatz, G. J., Mu, M., Kasibhatla, P. S.,
815 Morton, D. C., DeFries, R. S., Jin, Y., and van Leeuwen, T. T.: Global fire emissions and the
816 contribution of deforestation, savanna, forest, agricultural, and peat fires (1997–2009),
817 *Atmospheric Chem. Phys.*, 10, 11707–11735, <https://doi.org/10.5194/acp-10-11707-2010>,
818 2010.
- 819 Wu, H., Taylor, J. W., Szpek, K., Langridge, J. M., Williams, P. I., Flynn, M., Allan, J. D.,
820 Abel, S. J., Pitt, J., Cotterell, M. I., Fox, C., Davies, N. W., Haywood, J., and Coe, H.:
821 Vertical variability of the properties of highly aged biomass burning aerosol transported over
822 the southeast Atlantic during CLARIFY-2017, *Atmospheric Chem. Phys.*, 20, 12697–12719,
823 <https://doi.org/10.5194/acp-20-12697-2020>, 2020.
- 824 Zhang, L., Sun, J. Y., Shen, X. J., Zhang, Y. M., Che, H., Ma, Q. L., Zhang, Y. W., Zhang, X.
825 Y., and Ogren, J. A.: Observations of relative humidity effects on aerosol light scattering in
826 the Yangtze River Delta of China, *Atmospheric Chem. Phys.*, 15, 8439–8454,
827 <https://doi.org/10.5194/acp-15-8439-2015>, 2015a.
- 828 Zhang, L., Sun, J. Y., Shen, X. J., Zhang, Y. M., Che, H., Ma, Q. L., Zhang, Y. W., Zhang, X.
829 Y., and Ogren, J. A.: Observations of relative humidity effects on aerosol light scattering in
830 the Yangtze River Delta of China, *Atmospheric Chem. Phys.*, 15, 8439–8454,
831 <https://doi.org/10.5194/acp-15-8439-2015>, 2015b.
- 832 Zhang, L., Segal-Rozenhaimer, M., Che, H., Dang, C., Sedlacek III, A. J., Lewis, E. R.,
833 Dobracki, A., Wong, J. P. S., Formenti, P., Howell, S. G., and Nenes, A.: Light absorption by

834 brown carbon over the South-East Atlantic Ocean, *Atmospheric Chem. Phys.*, 22, 9199–
835 9213, <https://doi.org/10.5194/acp-22-9199-2022>, 2022.

836 Zhang, Q., Jimenez, J. L., Canagaratna, M. R., Allan, J. D., Coe, H., Ulbrich, I., Alfarra, M.
837 R., Takami, A., Middlebrook, A. M., Sun, Y. L., Dzepina, K., Dunlea, E., Docherty, K.,
838 DeCarlo, P. F., Salcedo, D., Onasch, T., Jayne, J. T., Miyoshi, T., Shimojo, A., Hatakeyama,
839 S., Takegawa, N., Kondo, Y., Schneider, J., Drewnick, F., Borrmann, S., Weimer, S.,
840 Demerjian, K., Williams, P., Bower, K., Bahreini, R., Cottrell, L., Griffin, R. J., Rautiainen,
841 J., Sun, J. Y., Zhang, Y. M., and Worsnop, D. R.: Ubiquity and dominance of oxygenated
842 species in organic aerosols in anthropogenically-influenced Northern Hemisphere
843 midlatitudes, *Geophys. Res. Lett.*, 34, <https://doi.org/10.1029/2007GL029979>, 2007.

844 Zieger, P., Fierz-Schmidhauser, R., Gysel, M., Ström, J., Henne, S., Yttri, K. E.,
845 Baltensperger, U., and Weingartner, E.: Effects of relative humidity on aerosol light
846 scattering in the Arctic, *Atmospheric Chem. Phys.*, 10, 3875–3890,
847 <https://doi.org/10.5194/acp-10-3875-2010>, 2010.

848 Zieger, P., Fierz-Schmidhauser, R., Weingartner, E., and Baltensperger, U.: Effects of
849 relative humidity on aerosol light scattering: results from different European sites,
850 *Atmospheric Chem. Phys.*, 13, 10609–10631, <https://doi.org/10.5194/acp-13-10609-2013>,
851 2013.

852 Zieger, P., Fierz-Schmidhauser, R., Poulain, L., Müller, T., Birmili, W., Spindler, G.,
853 Wiedensohler, A., Baltensperger, U., and Weingartner, E.: Influence of water uptake on the
854 aerosol particle light scattering coefficients of the Central European aerosol, *Tellus B Chem.*
855 *Phys. Meteorol.*, 66, 22716, <https://doi.org/10.3402/tellusb.v66.22716>, 2014.

856 Zieger, P., Aalto, P. P., Aaltonen, V., Äijälä, M., Backman, J., Hong, J., Komppula, M.,
857 Krejci, R., Laborde, M., Lampilahti, J., de Leeuw, G., Pfüller, A., Rosati, B., Tesche, M.,
858 Tunved, P., Väänänen, R., and Petäjä, T.: Low hygroscopic scattering enhancement of boreal
859 aerosol and the implications for a columnar optical closure study, *Atmospheric Chem. Phys.*,
860 15, 7247–7267, <https://doi.org/10.5194/acp-15-7247-2015>, 2015.

861